## Supplementary Information

# Ultrathin Defective $Fe_2O_{3-x}$ Skins on Exsolved Nanoparticles from Perovskite Cathode Enable Highly Active and Sulfur-Tolerant $CO_2$ Electroreduction

*Sehun Choi*[1,†], *Jungseub Ha*[1,†], *Sanghwa Jeong*[2], *Hansol Bae*[1], *Jeongbin Cho*[1], *Sujin Kim*[1], *Yongju Yun*[1], *Won Bae Kim*[1,2,*]

[1] Department of Chemical Engineering, Pohang University of Science and Technology (POSTECH), 77 Cheongam-ro, Nam-gu, Pohang-si, Gyeongsangbuk-do 37673, Republic of Korea

[2] Department of Battery Engineering, Graduate Institute of Ferrous & Eco Materials Technology (GIFT), Pohang University of Science and Technology (POSTECH), 77 Cheongam-ro, Nam-gu, Pohang-si, Gyeongsangbuk-do 37673, Republic of Korea

* E-main address: kimwb@postech.ac.kr (W. B. Kim)

† S. C. and J. H. Contributed equally to this paper

## Experimental Section

### Material synthesis

The SPFNM powder was synthesized using a modified a sol-gel process. Stoichiometric amounts of metal precursors, $Sr(NO_3)_2$ (Sigma-Aldrich, 99.0%), $Pr(NO_3)_3 \cdot 6H_2O$ (Sigma-Aldrich, 99.9%), $Fe(NO_3)_3 \cdot 9H_2O$ (Sigma-Aldrich, 98%), $Ni(NO_3)_2 \cdot 6H_2O$ (Samchun, 98%) $(NH_4)_6 \cdot Mo_7O_{24} \cdot 4H_2O$ (Sigma-Aldrich, 99%), were fully dissolved in deionized (DI) water. Citric acid (anhydrous, Daejung) and ethylenediaminetetraacetic acid (EDTA, Sigma-Aldrich, 99.5%) were subsequently added as chelating agents. The pH of the solution was adjusted to the range of 7-8 using aqueous ammonia. The mixture was then heated at 90 °C on a hot plate under vigorous stirring until a blackish-purple gel was obtained. This gel was dehydrated at 200 °C for 1 h, and then ground into a fine powder, and calcined at 1100 °C for 5 hours in ambient air to yield the final SPFNM product. For comparison purposes, $Sr_{2.0}Fe_{1.5}Mo_{0.5}O_{6-\delta}$ (SFM) was also prepared via a sol-gel method. The metal precursors used included $Sr(NO_3)_2$ (Sigma-Aldrich, 99.0%), $Fe(NO_3)_3 \cdot 9H_2O$ (Sigma-Aldrich, 98%), $(NH_4)_6 \cdot Mo_7O_{24} \cdot 4H_2O$ (Sigma-Aldrich, 99%), and chelating agents; citric acid, EDTA were dissolved, and synthesis procedure followed the same routes as described for SPFNM. Subsequently, the sample was reduced at 850 °C for 2 h under either humidified $H_2$ (5% $H_2O$) and pure $H_2$ at a total flow rate of 50 mL $min^{-1}$ to produce samples designated wet-SPFNM and dry-SPFNM, respectively.

### Cell fabrication

Electrolyte-supported solid oxide cells were fabricated for electrochemical performance evaluation. A button-type $La_{0.8}Sr_{0.2}Ga_{0.8}Mg_{0.2}O_{3-\delta}$ (LSGM, Fuel cell materials) electrolyte pellet was prepared via a dry-pressing method, followed by sintering in air at 1200 °C for 3 h and subsequently at 1450 °C for 10 h. The resulting dense LSGM pellet exhibited a diameter of 17 mm and a thickness of approximately 210 μm. For cathode preparation, the synthesized

SPFNM powder was mixed with a gadolinium-doped ceria (GDC, $Ce_{0.9}Gd_{0.1}O_2$, UHSA, AnanKasei) in a weight ratio of 6 : 4 using a planetary ball mill operated at 350 rpm for 2 h. The composite powder was then blended with an organic binder solution (ethyl cellulose dissolved in α-terpineol) in a 1.0 : 1.1 weight ratio and then ink was applied onto one side of the LSGM pellet via a screen-printing technique to form the cathode layer. The anode catalyst, $La_{0.6}Sr_{0.4}Co_{0.2}Fe_{0.8}O_3$ (LSCF, Fuel cell materials), was composited with GDC using the same method as the cathode. The resulting ink was screen-printed onto the opposite side of the electrolyte pellet to form the anode layer. After electrode coating, the assembled cell was calcined at 1000 °C for 2 h in air. The final porous electrodes exhibited a thickness of approximately 21 μm with an active area of 0.283 $cm^2$, and were firmly adhered to the LSGM electrolyte surface

**Material characterization**

X-ray diffraction (XRD) patterns were collected on a Rigaku Ultima IV diffractometer (40 kV, 30 mA). The crystal structures of SFM, SPFNM, and the SPFNM-GDC composite were determined, and phase fractions were identified and quantified by Rietveld refinement using Profex software. The measurements were conducted over a 2θ range of 20-80 °. The surface morphology and elemental distribution of the electrode catalysts were examined using field-emission scanning electron microscopy (FE-SEM, JSM 7800F PRIME, JEOL Ltd.) combined with energy-dispersive X-ray spectroscopy (EDS). Cross-sectional images of solid oxide cells were acquired using a SEM (SNE-4000M, SEC). Transmission electron microscopy (TEM, JEM-2200FS, JEOL) coupled with EDS and electron energy loss spectroscopy (EELS) was employed at an accelerating voltage of 200 kV to characterize the microstructure and elemental composition of the exsolved nanoparticles.

Areal surface coverage (θ) was estimated by assuming circular nanoparticles:

$$\theta = \frac{\sum \pi \cdot r^2}{A} = \rho \cdot \pi \cdot \frac{d_2}{4}$$

Interfacial line density (L) was defined as the total nanoparticle perimeter per unit area:

$$L = \frac{\sum 2\pi r}{A} = \rho \cdot \pi \cdot d$$

where ρ is the particle density (particles $\mu m^{-2}$), d is the mean particle diameter, and A is 1 $\mu m^2$). $CO_2$ temperature-programmed desorption ($CO_2$-TPD) analysis was conducted using a BELCAT II system (MicrotracBEL) to evaluate the $CO_2$ adsorption and desorption behavior. Prior to measurement, samples were pretreated in pure $CO_2$ at 200 °C for 1 h, followed by desorption under pure Ar flow from 25 °C to 800 °C at a ramp rate of 10 °C $min^{-1}$. Raman spectroscopy (HEDA, WEVE) with a 532 nm laser was utilized to identify sulfur species present in the treated samples. Soft X-ray absorption spectroscopy (XAS) was conducted on the 2A MS beamline at the Pohang Light Source (PLS-II) to investigate the surface electronic structure and oxidation states of Ni and Fe. *L*-edge spectra were collected in total electron yield (TEY) mode with an energy resolution of 0.1 eV. In situ synchrotron X-ray powder diffraction measurements were performed at the 3D-XRS beamline of PLS-II to investigate the structural reversibility of the SPFNM material. The X-ray beam, sourced from a bending magnet, was monochromated to a wavelength of 0.6884 Å (corresponding to 18.0 keV), and diffraction data were recorded with the detector positioned 344.6 mm from the sample. X-ray absorption fine structure (XAFS) analysis was conducted at the 8C and 10C beamlines of PLS-II to probe the electronic structure and reducibility of transition metal cations. X-ray absorption near edge structure (XANES) and Extended X-ray absorption fine structure (EXAFS) data were analyzed using Athena software. X-ray photoelectron spectroscopy (XPS) analysis was performed at the 10A2 beamline of PLS-II under ultra-high vacuum conditions (~$10^{-9}$ Torr). The O 1s, Fe 3p, C 1s, S 2p core levels were measured using a photon energy of 650 eV, while the Ni 2p core level was measured at 1100

eV. The energy scale was calibrated to the Au 4f peak of a reference Au foil, and all spectra were calibrated to the C 1s peak at 284.6 eV.

**Electrochemical measurements**

An electrolyte-supported button cell with an SPFNM-GDC|LSGM|LSCF-GDC configurations were utilized for SOEC testing. The cell was sealed into an alumina tube with ceramic adhesive (552-VFG, AREMCO), and silver paste, and wire were applied as current collectors. Prior to electrochemical testing, the cathode was pre-reduced under different atmospheres at 850 °C for 2 h to simulate varying exsolution environments: (i) pure $H_2$ for dry-SPFNM and (ii) humidified $H_2$ (5% $H_2O$) for wet-SPFNM. Subsequent electrochemical performance tests were conducted under simulated $CO_2$-separated blast furnace gas ($CO_2$-separated BFG) conditions. Here, "$CO_2$-separated BFG" denotes a pressure swing adsorption (PSA)-derived $CO_2$-enriched FINEX off-gas stream ($CO_2$-rich tail gas) envisioned after upstream gas conditioning (including primary desulfurization), rather than untreated raw BFG. Untreated BFG typically contains substantially lower $CO_2$ levels (20-30%), whereas $CO_2$ separation in FINEX-based capture schemes (e.g., PSA) can yield $CO_2$-enriched streams with $CO_2$ fraction comparable to the values adopted here.[1-4] The total gas flow rate was fixed at 50 ml $min^{-1}$, and measurements were performed at 850, 800, 750, 700 °C. The $CO_2$-separated BFG mixture consisted of $CO_2$ (69 mol%), CO (18 mol%), $H_2$ (5.3 mol%), $N_2$ (3.7 mol%), $H_2O$ (3 mol%), and $CH_4$ (1 mol%), with trace impurities of $H_2S$ (30 ppm) and $C_6H_6$ (500 ppm). Electrochemical impedance spectroscopy (EIS) measurements were performed using a Zivelab MP2 system, with a voltage amplitude of 28.3 mV in the frequency range from 100 MHz to 10 mHz, under both open circuit voltage (OCV) and applied voltage conditions. For long-term stability, chronopotentiometric tests were conducted under a constant current density of 250 mA $cm^{-2}$, tracking the voltage over 100 h with $CO_2$-separated BFG feed. To gain deeper insights into the electrode kinetics, distribution of relaxation times (DRT) analysis was performed using

DRTtools, a MATLAB based DRTtools developed by Ciucci's group.[5] Gas chromatography (Agilent 7890B) equipped with a 60/80 Carboxen 1000 column and a thermal conductivity detector (TCD) was employed to analyze the gaseous products from $CO_2$ electrolysis, enabling the calculation of CO production rate and Faradaic efficiency was calculated as:

$$FE\ (\%) = \frac{R_{CO,\,measured}}{R_{CO,\ theorectical}} \times 100\%$$

$$R_{CO,\,measured} = R_{CO,\,outlet} - R_{CO,inlet}$$

$$R_{CO,\,theorectical} = \frac{j}{z \times F}$$

Where F is the Faraday constant (96485 C $mol^{-1}$) and z is the electron stoichiometry, a value of 2 for $CO_2$ electrolysis.

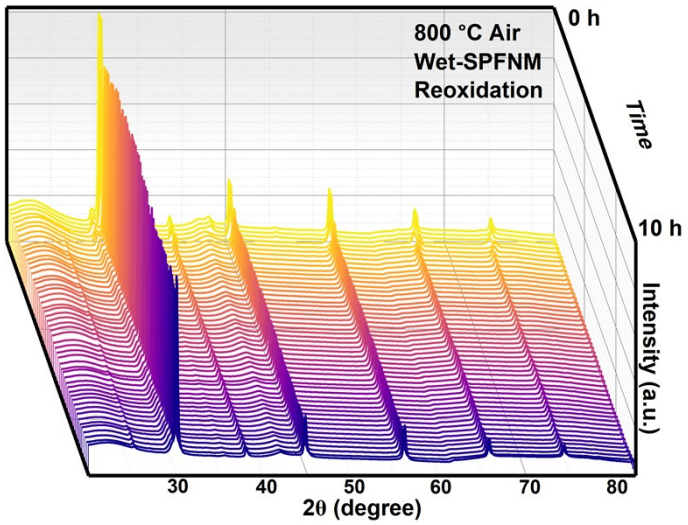


**Fig. S1**. In-situ XRD patterns of wet-SPFNM in the range of 20-80 º acquired at 800 ºC during 10 h reoxidation process.

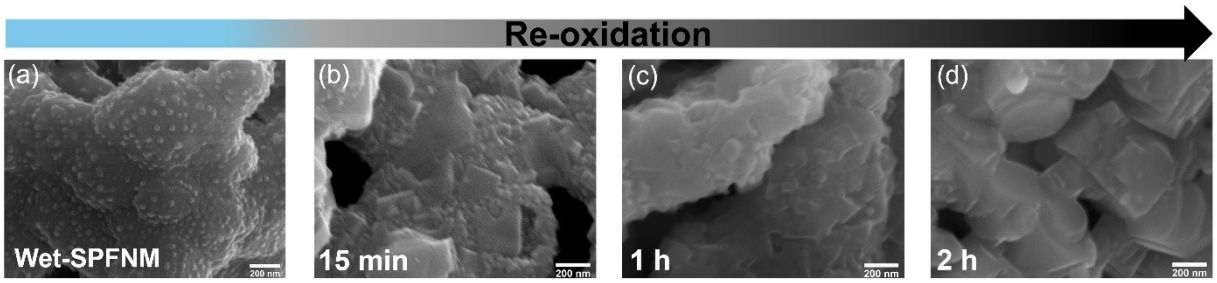


**Fig. S2**. SEM images of wet-SPFNM: (a) after wet reduction and after reoxidation for (b) 15 min, (c) 1h, (d) 2h.

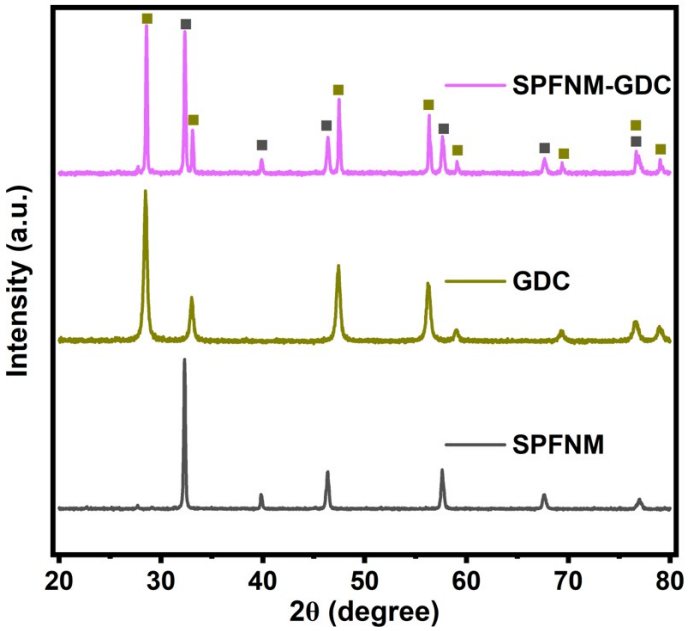


**Fig. S3**. XRD patterns of SPFNM-GDC composite annealed in ambient air at 1100 ºC for 2 h.

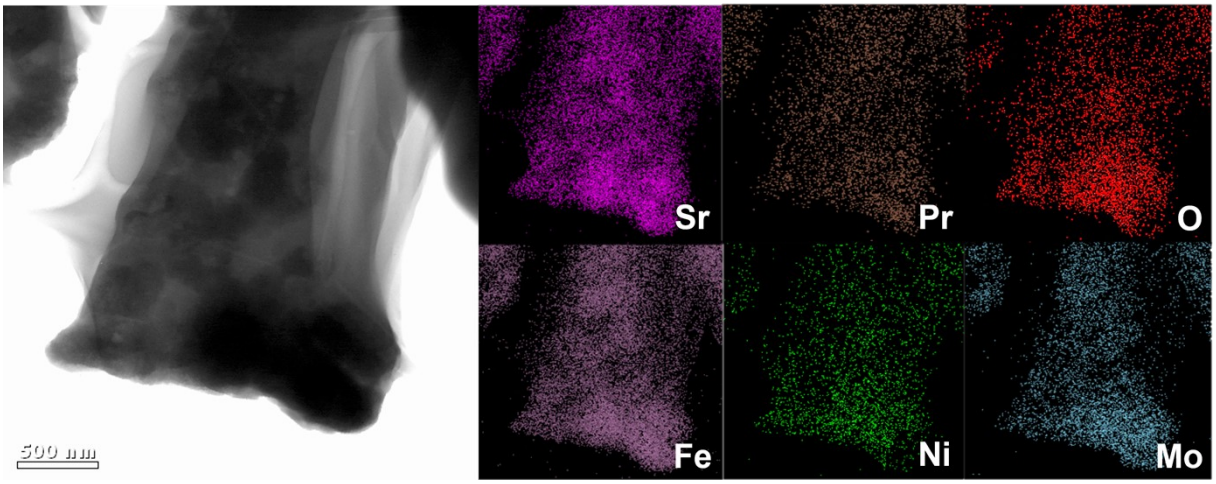


**Fig. S4**. STEM image and the corresponding EDS element mapping images of as-prepared SPFNM.

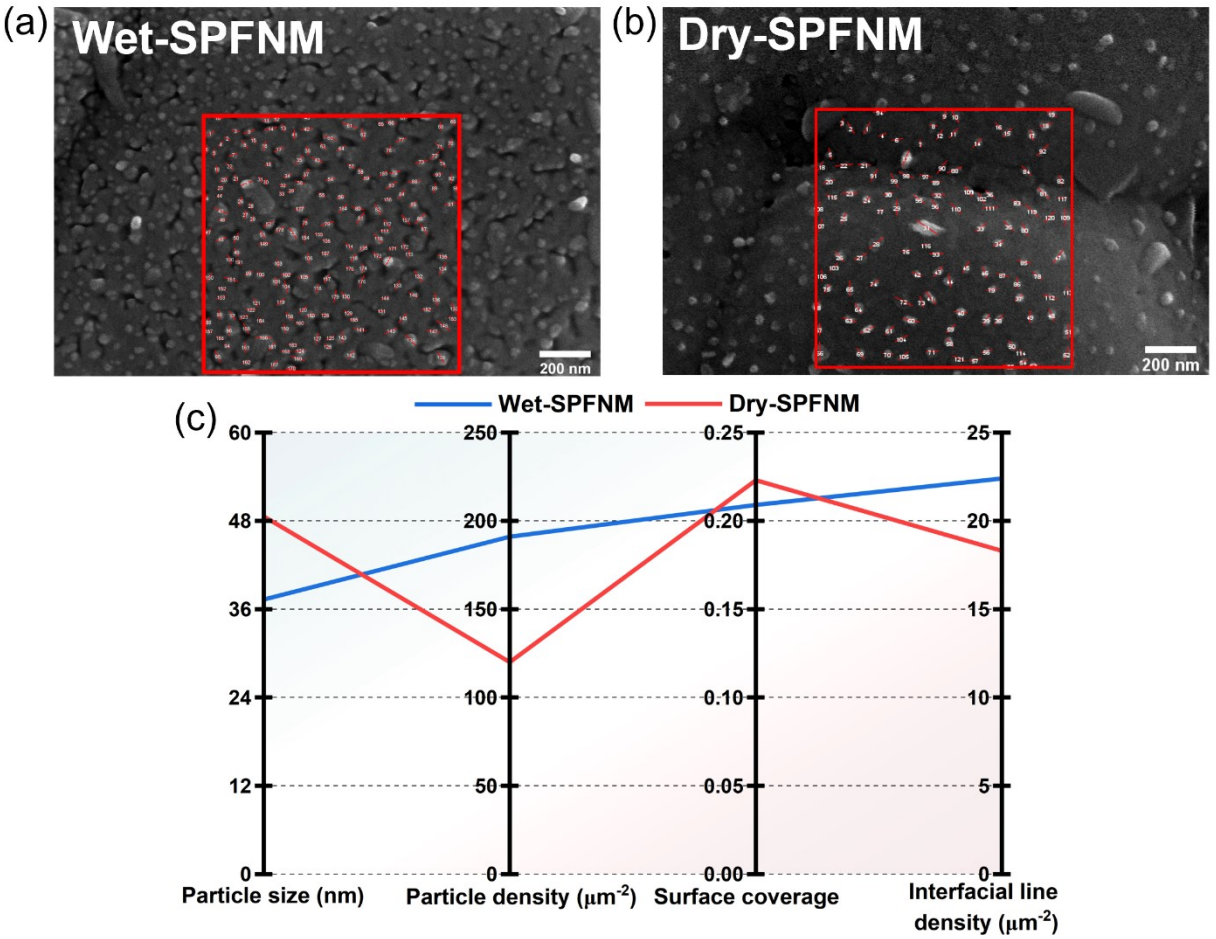


**Fig. S5**. SEM images and statistical comparison of exsolved nanoparticles on wet-SPFNM and dry-SPFNM. (a, b) Analyzed regions are highlighted (red squares). (c) Parallel-coordinates plot comparing particle size, particle density, surface coverage, interfacial line density.

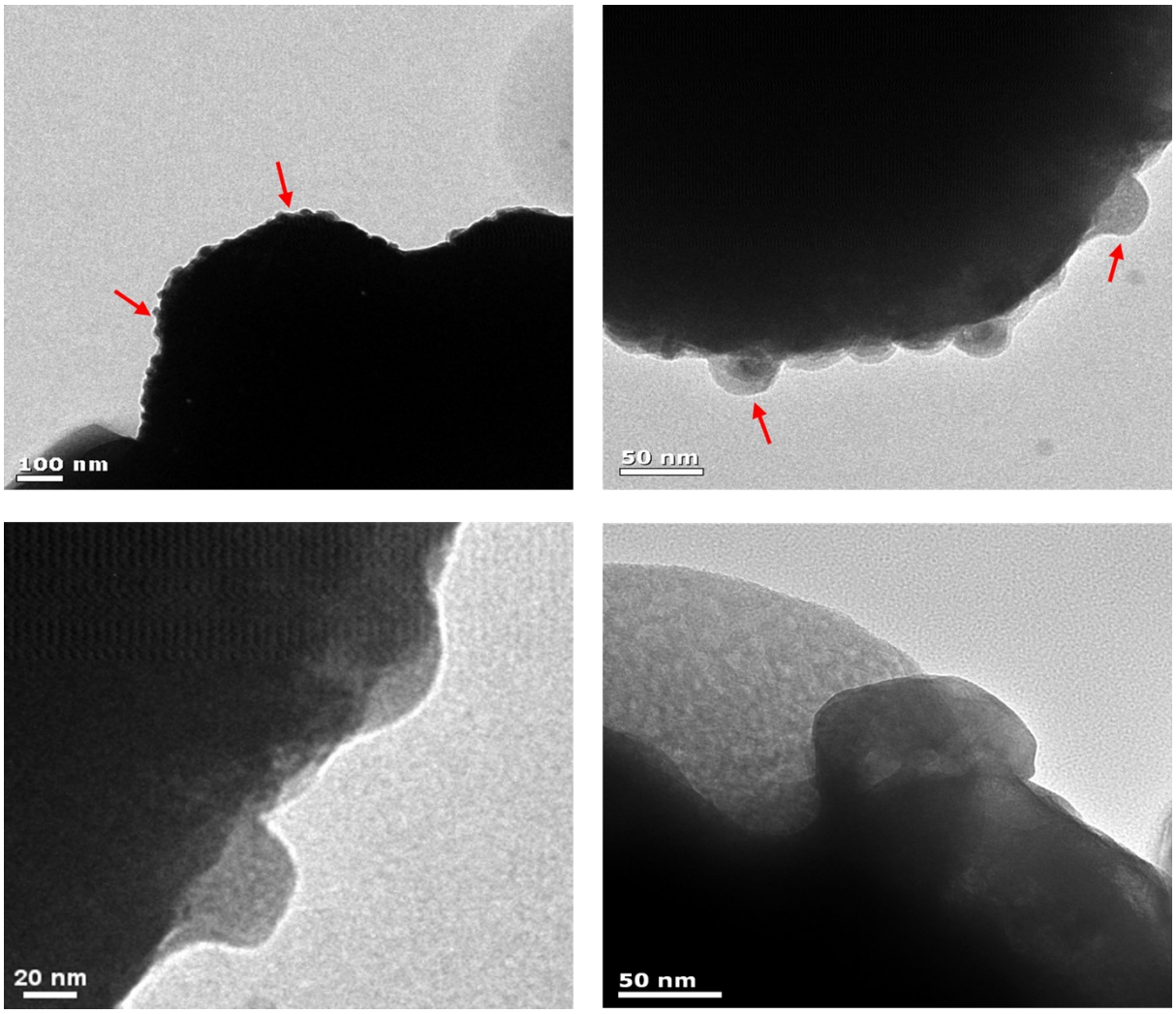


**Fig. S6**. TEM and High-resolution TEM (HR-TEM) images of dry-SPFNM at various magnifications.

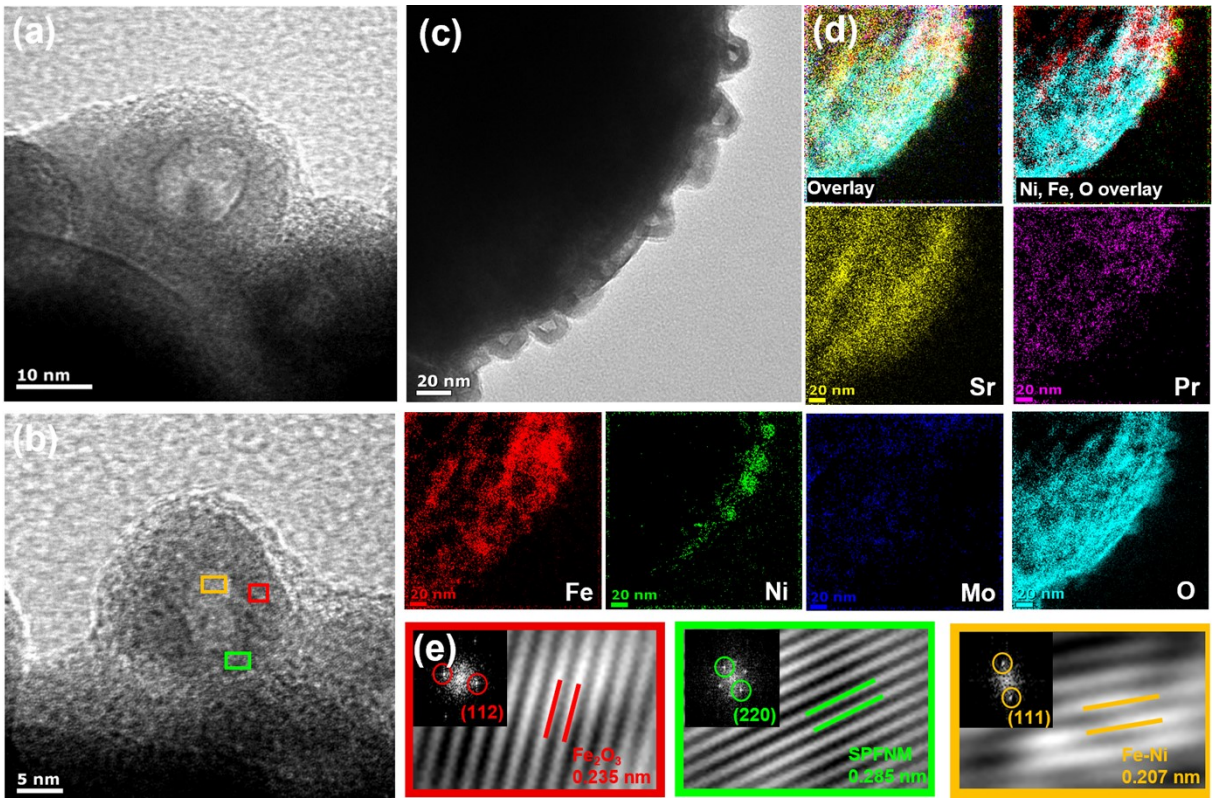


**Fig. S7**. (a, b) High-resolution images of exsolved core-shell nanoparticles under harsh humidified $H_2$ (~12% $H_2O$) atmosphere with corresponding (e) FFT and inverse FFT images of the spots and (c) TEM image and (d) corresponding EELS mapping at the Sr L-edge, Pr L-edge, Fe K-edge, Ni K-edge, Mo K-edge, O K-edge, respectively.

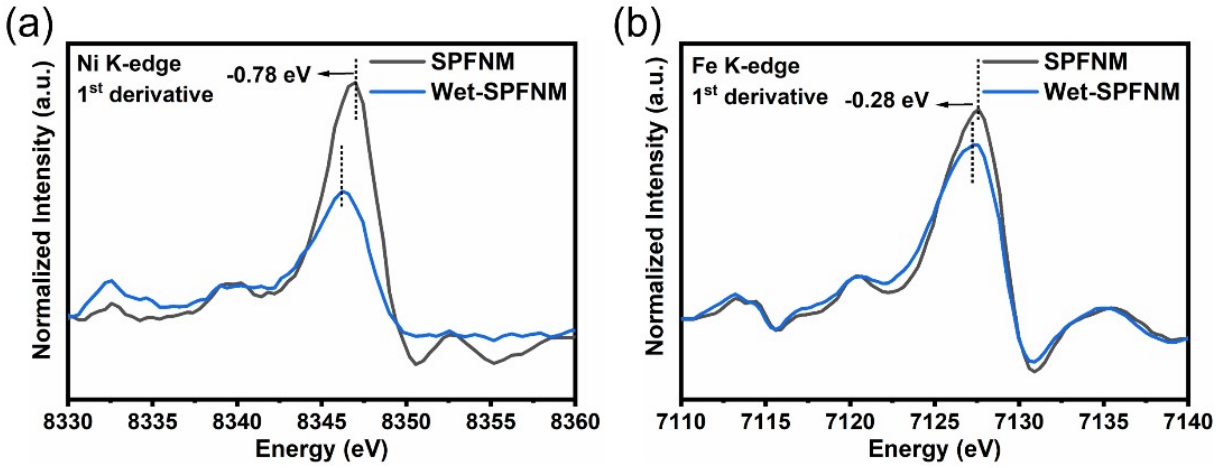


**Fig. S8**. The 1st derivatives of XANES spectra of (a) Ni K-edge (b) Fe K-edge for SPFNM and wet-SPFNM.

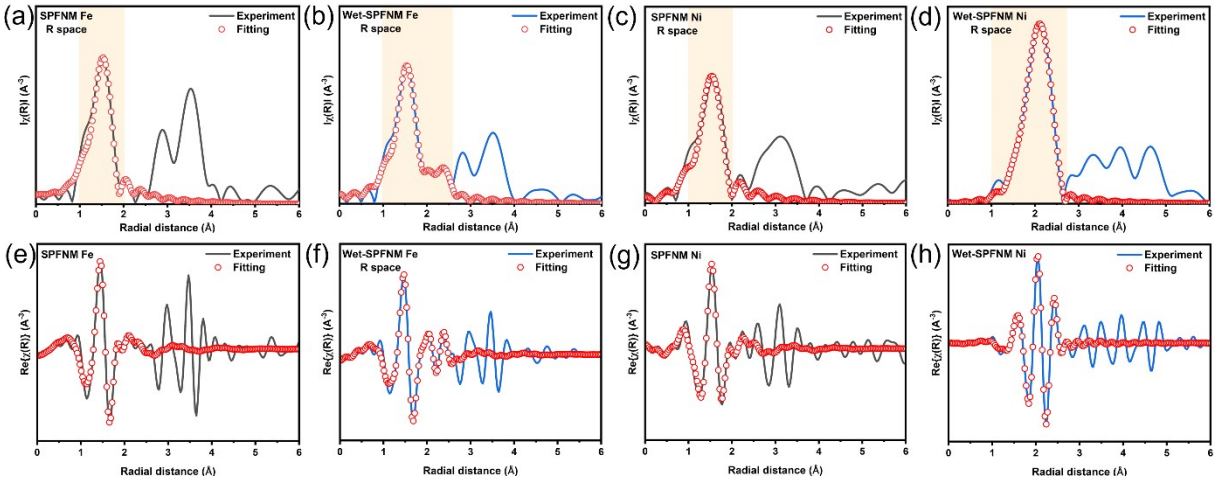


**Fig. S9**. Experimental and fitted EXAFS spectra of SPFNM and wet-SPFNM at the Fe and Ni K-edges. Fe K-edge $k^2$-weighted for (a) SPFNM and (b) wet-SPFNM. Ni K-edge $k^2$- weighted for (c) SPFNM and (d) wet-SPFNM. (e-h) Real part of the Fourier transforms in R-space and the corresponding fits.

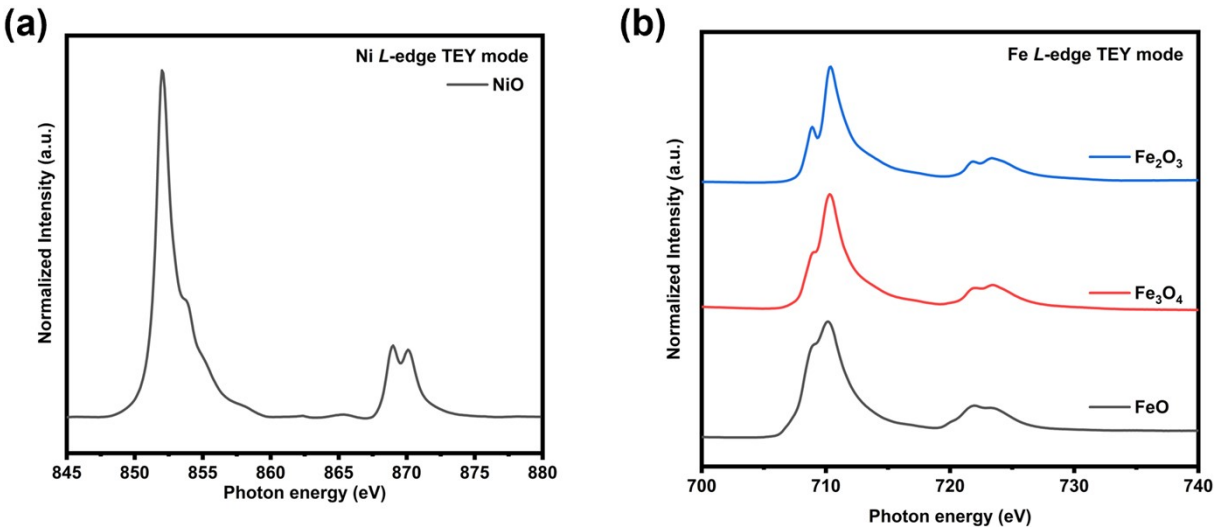


**Fig. S10**. Normalized XAS spectra of (a) NiO and (b) Fe oxide references in TEY mode.

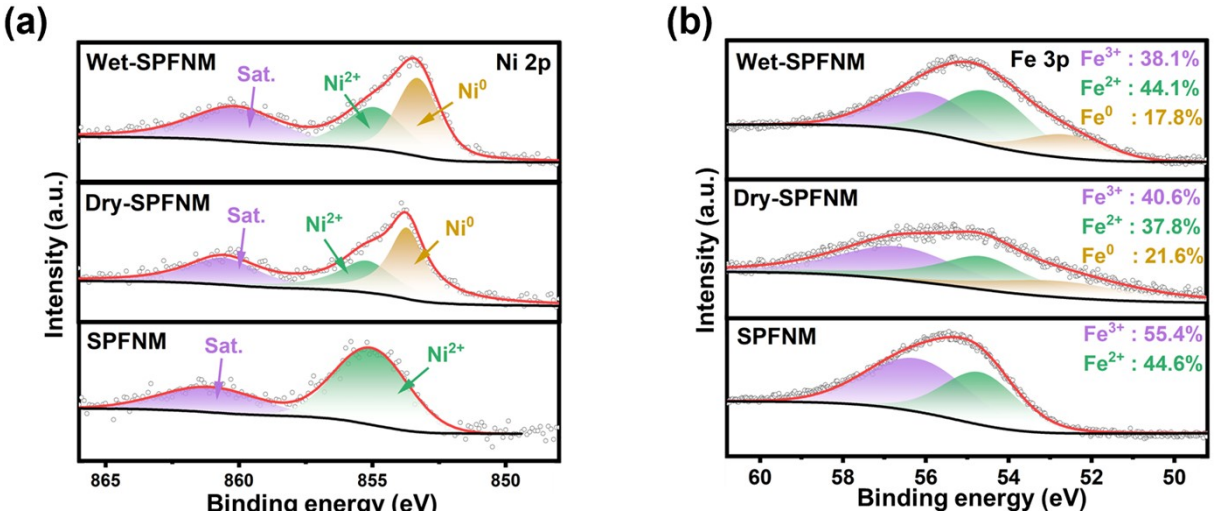


**Fig. S11**. XPS spectra of (a) Ni 2p, (b) Fe 3p for SPFNM, wet-SPFNM, dry-SPFNM.

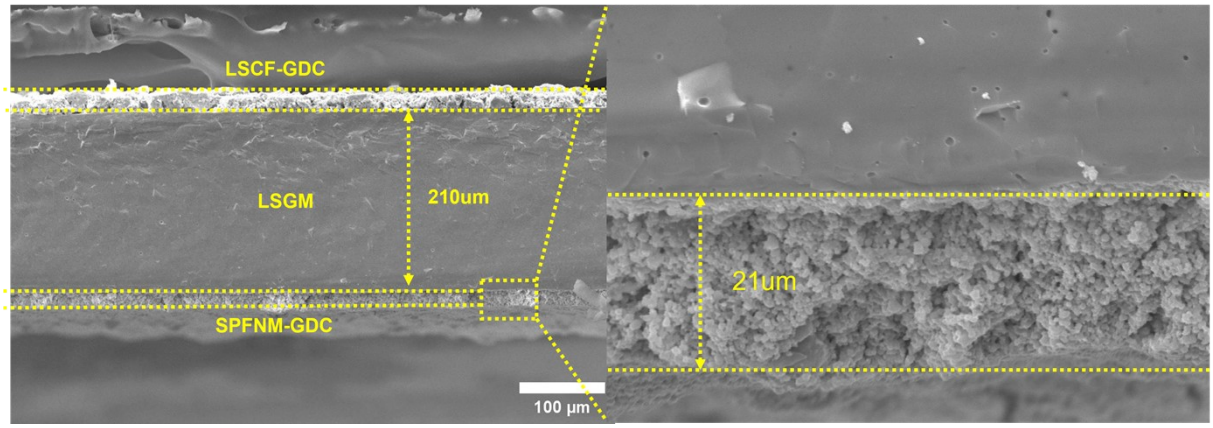


**Fig. S12**. Cross-sectional images of SPFNM single cell.

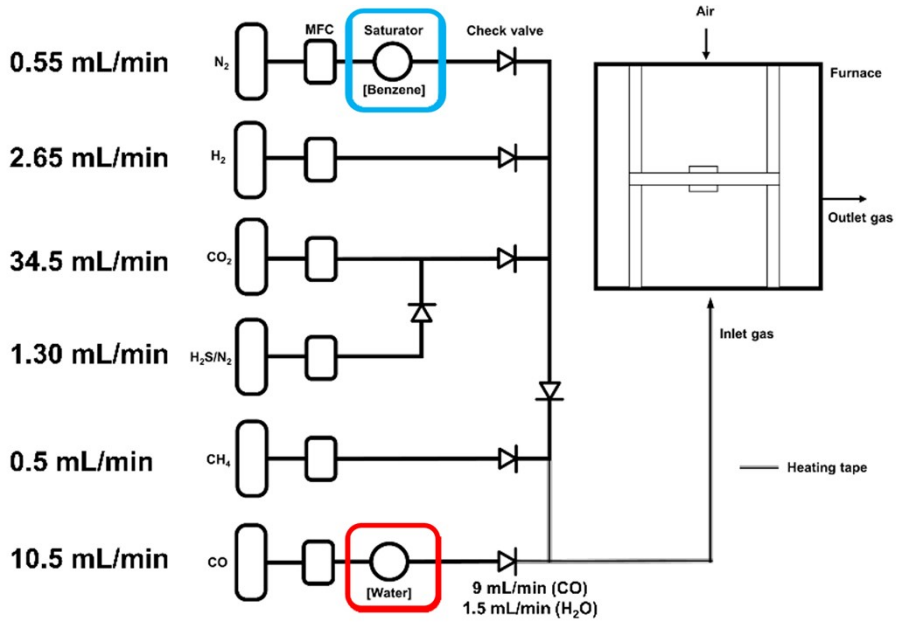


**Fig. S13**. Schematic of the simulated $CO_2$-separated BFG supply system and SOEC reactor.

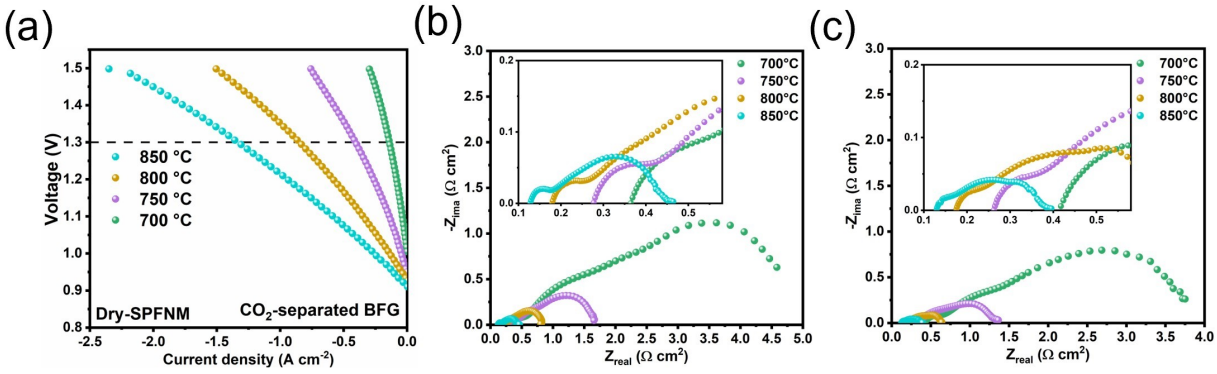


**Fig. S14**. (a) I-V curves and (b, c) Nyquist plots of the (b) dry-SPFNM, (c) wet-SPFNM cathode single cells at 850-700 °C.

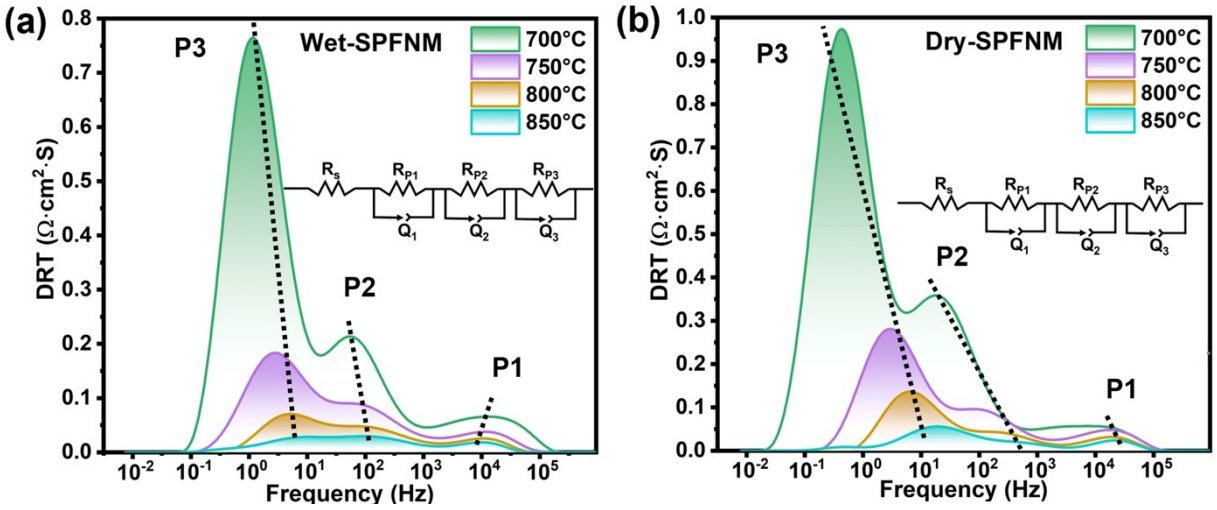


**Fig. S15**. DRT analysis of the wet-SPFNM and dry-SPFNM cathode single cells under $CO_2$-separated BFG atmosphere at 850-700 ˚C.

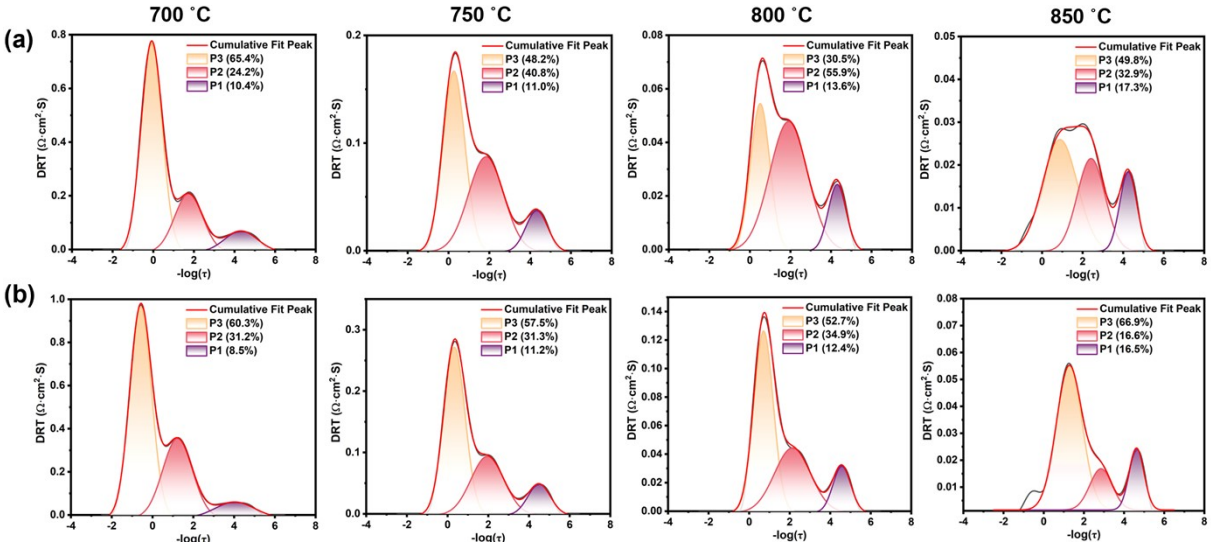


**Fig. S16**. Deconvoluted DRT plots of wet-SPFNM and dry-SPFNM at 850-700 ˚C.

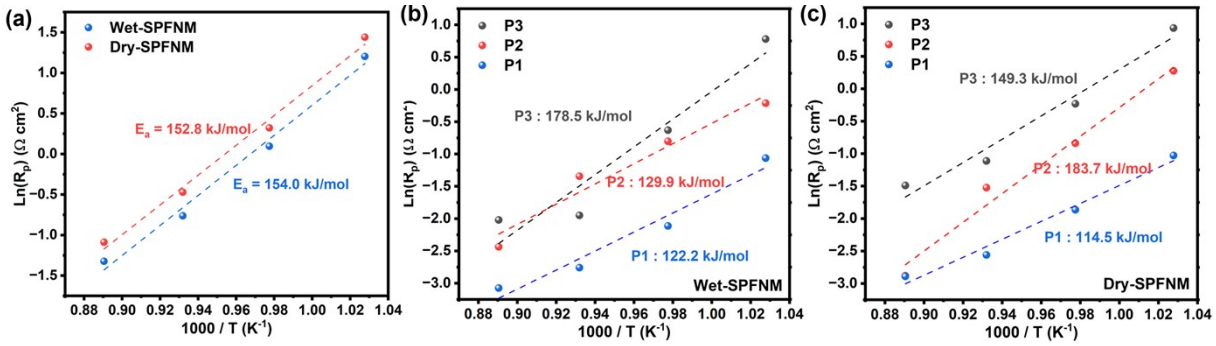


**Fig. S17**. (a) Arrhenius plots for the $R_p$ values and (b, c) individual polarization resistances (P1, P2, P3) derived from the deconvoluted DRT peaks.

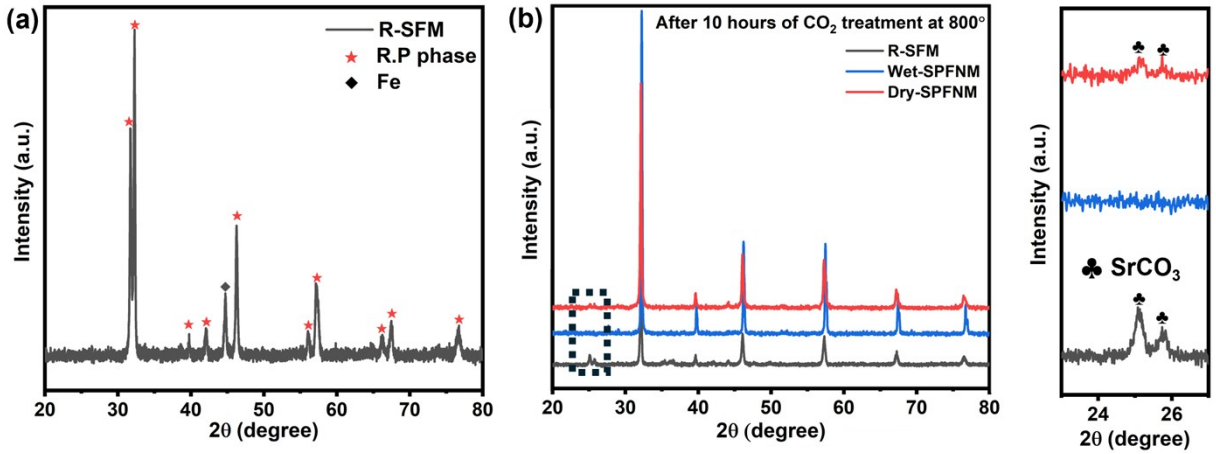


**Fig. S18.** (a) XRD pattern of reduced SFM ($Sr_{2.0}Fe_{1.5}Mo_{0.5}O_{6-\delta}$, designated as R-SFM); (b) XRD patterns of R-SFM, wet-SPFNM, dry-SPFNM after $CO_2$ treatment for 10 h at 800 °C.

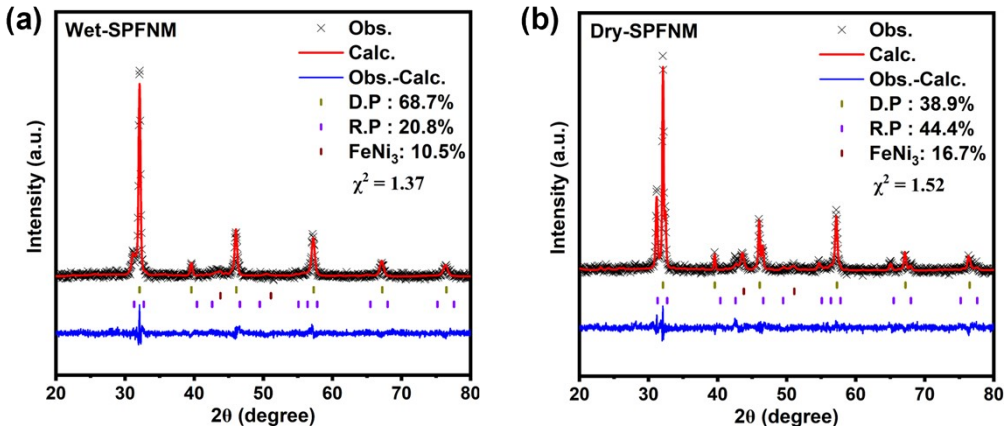


**Fig. S19.** X-ray diffraction Rietveld refinements of wet-SPFNM and dry-SPFNM.

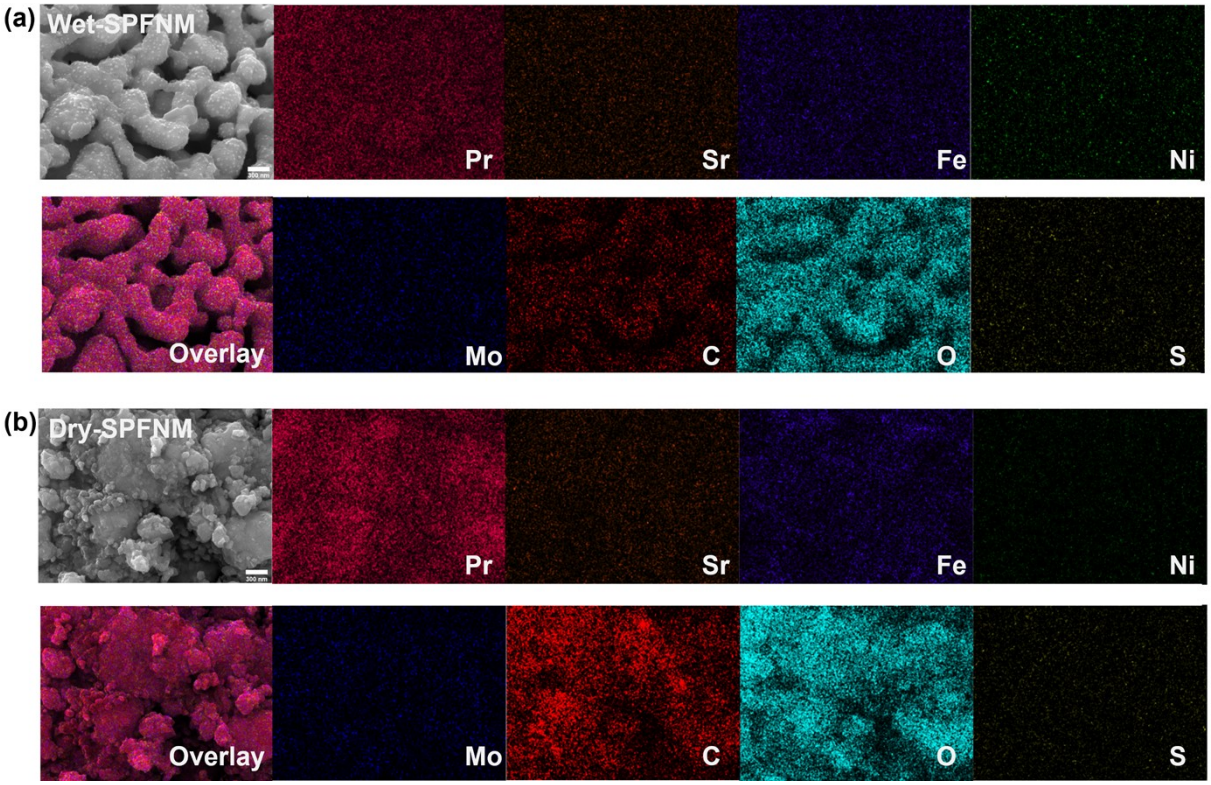


**Fig. S20**. SEM-EDS analysis of (a) wet-SPFNM and (b) dry-SPFNM after 10 h treatment at 750 ºC in $CO_2$-separated BFG conditions.

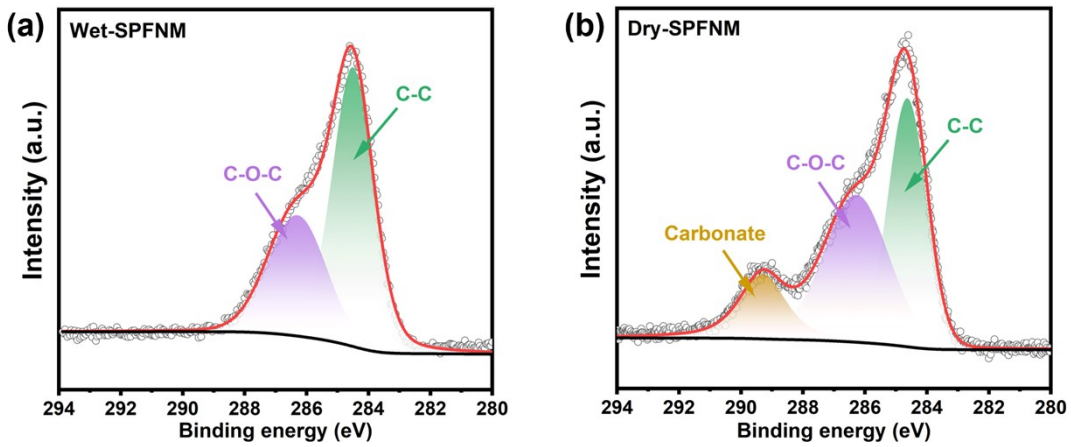


**Fig. S21**. XPS spectra of C 1s for (a) wet-SPFNM, (b) dry-SPFNM after 10 h treatment at 750 ºC in $CO_2$-separated BFG conditions.

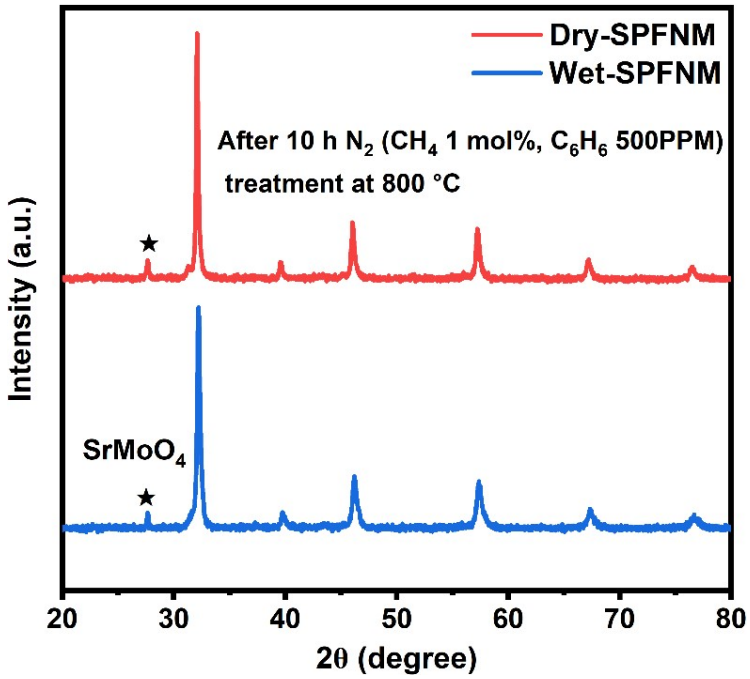


**Fig. S22**. XRD pattern of wet-SPFNM and dry-SPFNM after 10 h treatment at 800 ºC in $N_2$ containing 1 mol% $CH_4$ and 500 ppm $C_6H_6$

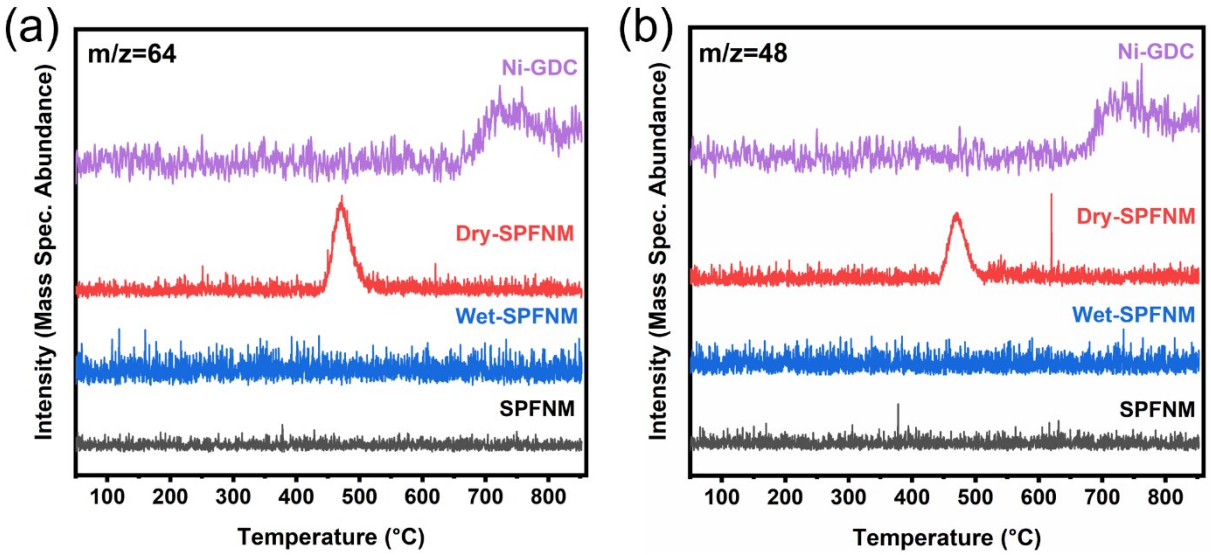


**Fig. S23**. $O_2$-TPO-MS profiles monitored at (a) *m/z* = 64 ($SO_2$) and (b) *m/z*=48 (SO) for SPFNM, wet-SPFNM, dry-SPFNM, and Ni-GDC after annealing in $CO_2$-separated BFG for 12 h at 750 °C.

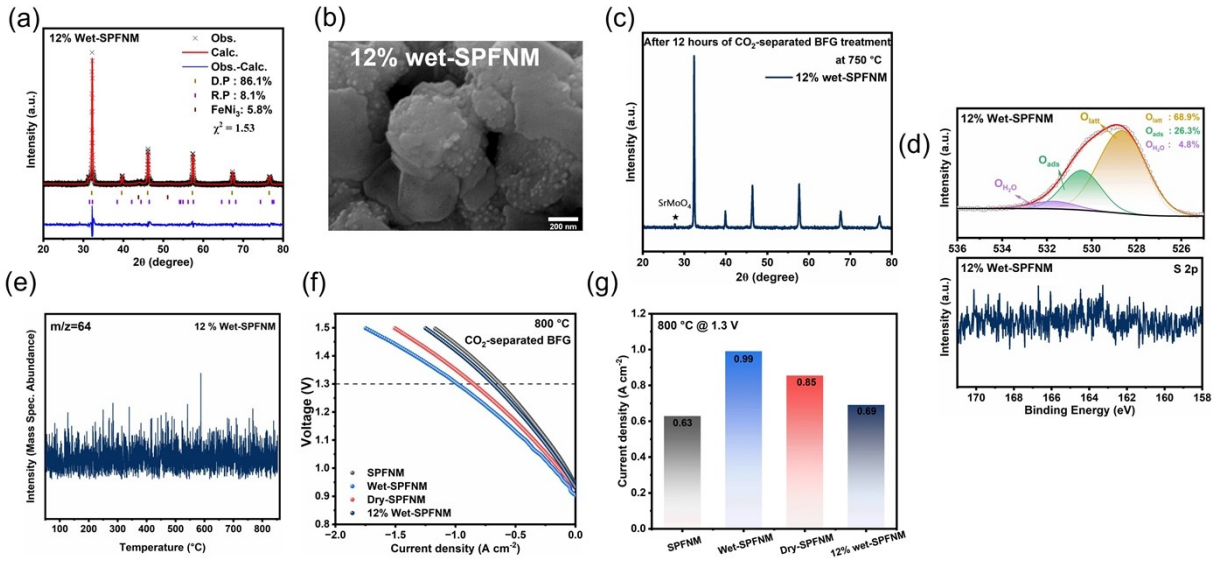


**Fig. S24**. Characterization and electrochemical performance of the 12% wet-SPFNM sample. (a) XRD pattern and Rietveld refinement. (b) SEM images. (c) XRD pattern after $CO_2$-separated BFG treatment. (d) O 1s XPS of the 12 % wet-SPFNM and S 2p XPS after $CO_2$-separated BFG treatment. (e) $O_2$-TPO-MS profile after $CO_2$-separated BFG treatment. (f) I-V curves at 800 °C for SPFNM, wet-SPFNM, dry-SPFNM, and 12% wet-SPFNM. (g) Current density at 1.3 V extracted from (f).

**Table S1.** Structural parameters extracted from the Fe K-edge and Ni K-edge EXAFS fitting.

| Sample | Path | CN | $\sigma^2$ (Å$^2$) | $\Delta E_0$ (eV) | R (Å) | R-factor |
|---|---|---|---|---|---|---|
| SPFNM | Fe-O | 5.2±0.8 | 0.0064±0.0022 | 3.5±2.1 | 1.941±0.0167 | 0.006 |
| | Ni-O | 5.3±1.0 | 0.0078±0.0029 | -2.7±2.4 | 1.995±0.0201 | 0.008 |
| Wet-SPFNM | Fe-O | 5.0±0.7 | 0.0064±0.0022 | 3.1±2.1 | 1.958±0.0164 | 0.005 |
| | Fe-Fe | 1.4±1.1 | 0.0090±0.0072 | 3.1±2.1 | 2.521±0.0243 | |
| | Ni-O | 2.6±0.6 | 0.0042±0.0031 | 3.9±2.4 | 2.088±0.0221 | 0.002 |
| | Ni-Ni | 8.2±1.1 | 0.0082±0.0011 | -4.7±1.4 | 2.507±0.0077 | |

· $S_0^2$ is fixed as 0.7, CN is the coordination number, R is the interatomic distance. $\sigma^2$ is Debye-Waller factor, $\sigma^2 \leq 0.01$. R factor is used to value the goodness of the fitting, R factor ≤ 0.02. $\Delta E_0$ is the inner potential correction, $|\Delta E_0| \leq 10$ eV.

**Table S2**. Peak intensity ratios ($e_g/t_{2g}$) of the Fe $L_3$-region for pristine SPFNM, wet-SPFNM, and dry-SPFNM.

| Materials | $t_{2g}$ | $e_g$ | $e_g/t_{2g}$ |
|---|---|---|---|
| **SPFNM** | 0.637 | 1.351 | 2.122 |
| **Wet-SPFNM** | 0.441 | 0.488 | 1.107 |
| **Dry-SPFNM** | 0.400 | 0.408 | 1.019 |
| **FeO** | 3.790 | 4.727 | 1.247 |
| **$Fe_3O_4$** | 1.209 | 2.458 | 2.033 |
| **$Fe_2O_3$** | 1.794 | 3.732 | 2.080 |

**Table S3**. The $R_p$ values of the single cells with pristine SPFNM, dry-SPFNM and wet-SPFNM cathodes, measured at 750 ˚C under applied voltages of 0.1-0.4 V (vs OCV).

| Rp ($\Omega$ $cm^2$) | **Pristine-SPFNM** | **Dry-SPFNM** | **Wet-SPFNM** |
|---|---|---|---|
| **0.1 V** | 1.425 | 1.116 | 0.947 |
| **0.2 v** | 0.930 | 0.734 | 0.547 |
| **0.3 V** | 0.831 | 0.597 | 0.497 |
| **0.4 V** | 0.761 | 0.523 | 0.474 |

**Table S4**. The resistances of the single cell with wet-SPFNM cathode at 700-850 ºC.

| | $R_s$(Ω $cm^2$) | $R_p$(Ω $cm^2$) | $R_t$(Ω $cm^2$) |
|---|---|---|---|
| **700 ºC** | 0.418 | 3.333 | 3.751 |
| **750 ºC** | 0.258 | 1.10 | 1.358 |
| **800 ºC** | 0.176 | 0.466 | 0.642 |
| **850 ºC** | 0.130 | 0.266 | 0.396 |

**Table S5.** The resistances of the single cell with dry-SPFNM cathode at 700-850 ºC.

| | $R_s$(Ω $cm^2$) | $R_p$(Ω $cm^2$) | $R_t$(Ω $cm^2$) |
|---|---|---|---|
| **700 ºC** | 0.365 | 4.219 | 4.584 |
| **750 ºC** | 0.278 | 1.379 | 1.657 |
| **800 ºC** | 0.181 | 0.624 | 0.805 |
| **850 ºC** | 0.128 | 0.337 | 0.465 |

**Table S6**. Performance comparison of cathodes in this study with those from previously reported $CO_2$ electrolysis studies conducted under $CO/CO_2$ mixed-gas and 100% $CO_2$ conditions at 1.5 V at 800 ºC.

| Cathode | Electrolyte (thickness) | Cell configuration | Test conditions | J (A $cm^{-2}$) 800 ºC @1.5 V |
|---|---|---|---|---|
| $FeNi_3/Fe_2O_{3-x}$@SPFNM (wet-SPFNM) | LSGM (210μm) | SPFNM-GDC\|LSGM\|LSCF-GDC | $CO_2$-separated BFG | 1.75 |
| $FeNi_3$@SPFNM (dry-SPFNM) | LSGM (210μm) | SPFNM-GDC\|LSGM\|LSCF-GDC | $CO_2$-separated BFG | 1.5 |
| QA@SFCNCM[6] | LSGM (230μm) | SFCNCM\|LDC\|LSGM\|LDC\|SFCNCM | 50% $CO/CO_2$ | 0.45 |
| Ni@LSTN[7] | YSZ (500μm) | LSTNn\|YSZ\|LSCF | 15% $CO/CO_2$ | 0.62 |
| NiFe@SFM[8] | LSGM (230μm) | SFNM\|SDC\|LSGM\|SDC\|SFMN | 70% $CO/CO_2$ | 1.07 |
| LSFM-Fe[9] | LSGM (200μm) | LSFM-Fe\|LSGM\|SSC | 50% $CO/CO_2$ | 1.49 |
| LSCM-CMF[10] | LSGM (200μm) | LSCM-CMF\|LDC\|LSGM\|SSC | 30% $CO/CO_2$ | 1.67 |
| LSCM@nano-CMF[11] | LSGM (200μm) | LSCM-CMF\|LDC\|LSGM\|SSC | 50% $CO/CO_2$ | 1.98 |
| FeNi@PBFN[12] | LSGM (300μm) | PBFN\|LSGM\|LSCF | 100% $CO_2$ | 1.09 |
| FeNi@BiSFNM[13] | LSGM (270μm) | BiSFNM\|LDC\|LSGM\|LSCF-GDC | 100% $CO_2$ | 1.30 |
| NiFe@SFVMNT[14] | LSGM (240μm) | SFVMNT\|SDC\|LSGM\|PBSCF-GDC | 100% $CO_2$ | 1.66 |
| Ni@Ni-SFM/Ni-GDC[15] | LSGM (270μm) | Ni-SFM/Ni-GDC\|LSGM\|PBSCF-GDC | 100% $CO_2$ | 1.72 |
| NiFe@FeOx/LSFN[16] | LSGM (260μm) | LSFN-GDC\|LDC\|LSGM\|LSCF-GDC | 100% $CO_2$ | 1.72 |
| CoFe@LSCC[17] | LSGM (500μm) | LSCC+Fe\|LDC\|LSGM\|LSCF-GDC | 100% $CO_2$ | 1.73 |
| CuFe@PSFCM[18] | LSGM (200μm) | PSFCM\|LSGM\|BSCF | 100% $CO_2$ | 1.97 |
| CuFe@SFCM[19] | LSGM (250μm) | SFCM\|LDC\|LSGM\|LSCF-SDC | 100% $CO_2$ | 2.5 |

## Reference


1 S-H. Yi, M-E. Choi, D-H. Kim, C-K. Ko, W-I. Park, S-Y. Kim, Ironmak. Steelmak., 2019, **46(7)**, 625-631.

2 A. Carpenter, IEA Clean Coal Centre, 2012, **25**, 193.

3 W. Jeong, J. Lee, C-K. Ko, S-H. Yi, J. H. Lee, Int. J. Greenh. Gas Control, 2023, **127**, 103926

4 S. Santos, IEAGHG Report, 2013

5 T. H. Wan, M. Saccoccio, C. Chen, F. Ciucci, *Electrochim. Acta*, 2015, **184**, 483-499.

6 Y. Luo, D. Zhang, T. Liu, X. Chang, J. Wang, Y. Wang, X.K. Gu and M. Ding, Adv. Funct. Mater., 2024, **34**, 2403922.

7 Z. Liu, J. Zhou, Y. Sun, X. Yue, J. Yang, L. Fu, Q. Deng, H. Zhao, C. Yin and K. Wu, J. Energy Chem., 2023, **84**, 219-227.

8 Y. Li, Y. Li, S. Zhang, C. Ren, Y. Jing, F. Cheng, Q. Wu, P. Lund and L. Fan, ACS Appl. Mater. Interfaces, 2022, **14**, 9138-9150.

9 S.W. Lee, T.H. Nam, M. Kim, S. Lee, K.H. Lee, J.H. Park and T.H. Shin, Inorg. Chem. Front., 2023, **10**, 3536-3543.

10 S. Lee, M. Kim, K.T. Lee, J.T. Irvine and T.H. Shin, Adv. Energy Mater., 2021, **11**, 2100339.

11 S.W. Lee, T.H. Nam, T. Ishihara, J.T. Irvine and T.H. Shin, Energy Environ. Sci., 2025, **18**, 1205-1213.

12 X. Wang, H. Hu, C. Xie, Y. Wang, H. Li and X. Ding, J. Mater. Chem. A, 2024, **12**, 11701-11709

13 M. Emadi and E. Croiset, J. Mater. Chem. A, 2026, Advance Article.

14 Y. Zhu, N. Zhang, W. Zhang, Y. Gong, R. Wang, H. Wang, J. Jin, L. Zhao and B. He, J. Mater. Chem. A, 2024, **12**, 18182-18192.

15 F. Hu, Y. Ling, S. Fang, L. Sui, H. Xiao, Y. Huang, B. He and L. Zhao, Appl. Catal. B-Environ., 2023, **337**, 122968.

16 L-B. Liu, S. Liu, M. Yang, Y. Li, B. Ouyang, P. Zhang, X-Z. Fu, Y. Sun, S. Liu and J.-L. Luo, Appl. Catal. B-Environ. Energy, 2025, **379**, 125705.

17 Y. Shen, S. Wang, X. Chen, H. Lv, Y. Guo, H. Liu, H. Zhao, N. Ta, M. Li, X. Zhang, Y. Song, G. Wang and X. Bao, J. Am. Chem. Soc. 2025, **147(35)**, 31821-31828.

18 D. Liu, H. Shang, C. Zhou, J. Miao, D. Xu, Z. Chen, M. Fei, F. Liang, Q. Niu, R. Ran, W. Zhou and Z. Shao, Energy Environ. Mater., 2024, **7(5),** e12717.

19 X. Xi, Y. Fan, J. Zhang, J.-L. Luo and X.-Z. Fu, *J. Mater. Chem. A*, 2022, **10**, 2509-2518